Life Cycles of Hurricane-Like Vorticity Rings

ERIC A. HENDRICKS,* WAYNE H. SCHUBERT, AND RICHARD K. TAFT

Colorado State University, Fort Collins, Colorado

HUIQUN WANG

Harvard–Smithsonian Center for Astrophysics, Cambridge, Massachusetts

JAMES P. KOSSIN

Cooperative Institute for Meteorological Satellite Studies, Madison, Wisconsin

(Manuscript received 23 April 2008, in final form 14 August 2008)

ABSTRACT

The asymmetric dynamics of potential vorticity mixing in the hurricane inner core are further advanced by examining the end states that result from the unforced evolution of hurricane-like vorticity rings in a nondivergent barotropic model. The results from a sequence of 170 numerical simulations are summarized. The sequence covers a two-dimensional parameter space, with the first parameter defining the hollowness of the vortex (i.e., the ratio of eye to inner-core relative vorticity) and the second parameter defining the thickness of the ring (i.e., the ratio of the inner and outer radii of the ring). In approximately one-half of the cases, the ring becomes barotropically unstable, and there ensues a vigorous vorticity mixing episode between the eye and eyewall. The output of the barotropic model is used to (i) verify that the nonlinear model approximately replicates the linear theory of the fastest-growing azimuthal mode in the early phase of the evolution, and (ii) characterize the end states (defined at $t = 48$ h) that result from the nonlinear chaotic vorticity advection and mixing. It is found that the linear stability theory is a good guide to the fastest-growing exponential mode in the numerical model. Two additional features are observed in the numerical model results. The first is an azimuthal wavenumber-2 deformation of the vorticity ring that occurs for moderately thick, nearly filled rings. The second is an algebraically growing wavenumber-1 instability (not present in the linear theory because of the assumed solution) that is observed as a wobbling eye (or the trochoidal oscillation for a moving vortex) for thick rings that are stable to all exponentially growing instabilities. Most end states are found to be monopoles. For very hollow and thin rings, persistent mesovortices may exist for more than 15 h before merging to a monopole. For thicker rings, the relaxation to a monopole takes longer (between 48 and 72 h). For moderately thick rings with nearly filled cores, the most likely end state is an elliptical eyewall. In this nondivergent barotropic context, both the minimum central pressure and maximum tangential velocity simultaneously decrease over 48 h during all vorticity mixing events.

1. Introduction

Diabatic heating in the core of a tropical storm tends to produce a tower of potential vorticity (PV) that extends into the upper troposphere (Schubert and Alworth 1987). As the storm strengthens into a hurricane and an eye forms, diabatic heating becomes confined to the eyewall region and this PV tower becomes hollow. This hollow tower structure (Möller and Smith 1994) has been recently simulated in a high-resolution full-physics model by Yau et al. (2004). The sign reversal of the radial gradient of PV sets the stage for dynamic instability. If the hollow tower is thin enough, it may break down, causing potential vorticity to be mixed into the eye. During these PV mixing episodes, polygonal eyewalls, asymmetric eye contraction, and eye mesovortices have been documented in numerical models, laboratory experiments, and observations (Schubert et al. 1999, hereafter SM99; Kossin and Schubert 2001; Montgomery

* Current affiliation: Marine Meteorology Division, Naval Research Laboratory, Monterey, California.

Corresponding author address: Eric A. Hendricks, Naval Research Laboratory, Monterey, CA 93943.
E-mail: eric.hendricks@nrlmry.navy.mil

DOI: 10.1175/2008JAS2820.1

© 2009 American Meteorological Society

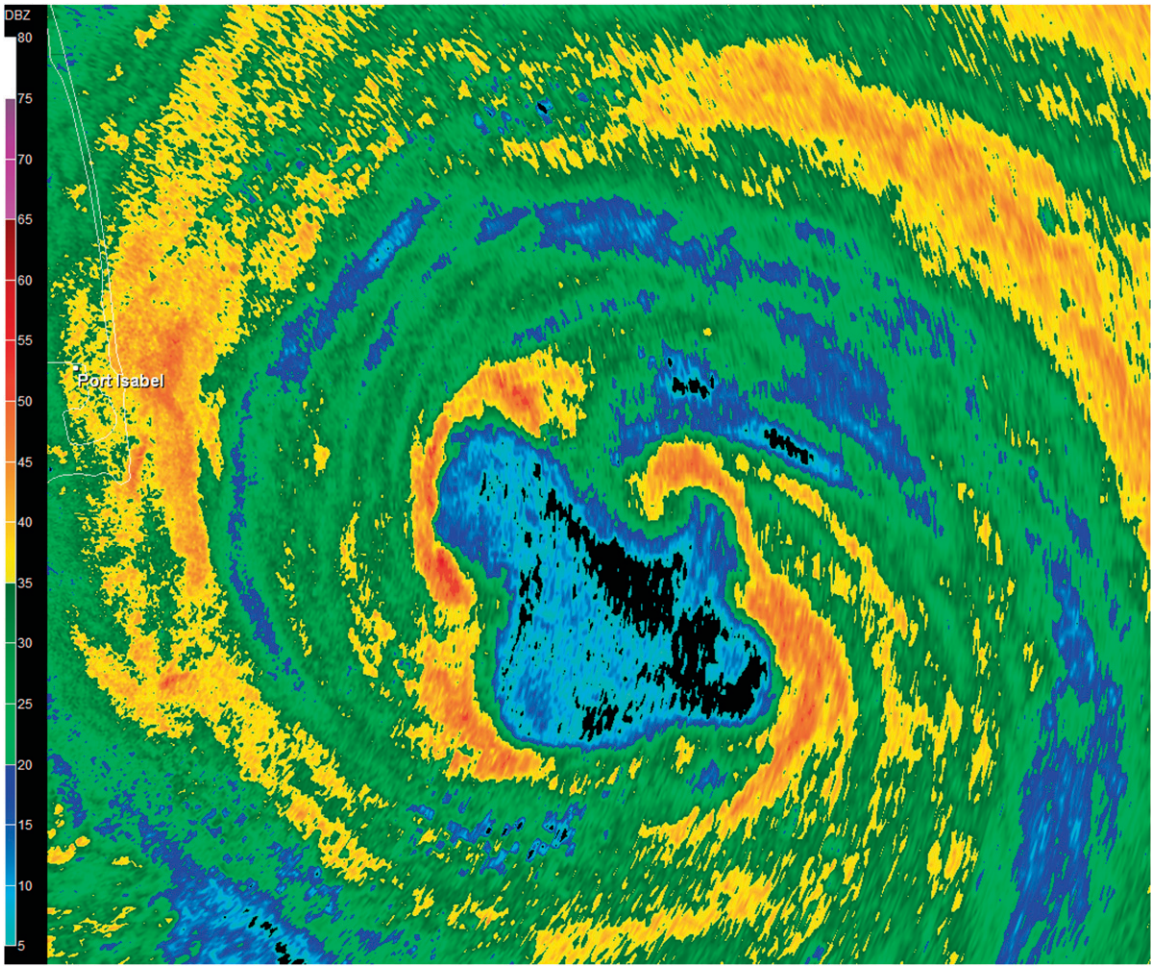

FIG. 1. Base reflectivity (left, dBZ color scale) from the Brownsville, TX, National Weather Service radar at 1052 UTC 23 Jul 2008. At this time Hurricane Dolly was approaching the coast and asymmetries, including eye mesovortices and straight line segments, were observed in the inner core.

et al. 2002; Kossin et al. 2002; Kossin and Schubert 2004). Eye mesovortices are sometimes visible in radar images or even in satellite images as vortical cloud swirls in the eye. As an example of mesovortices and inner-core vorticity mixing, a radar reflectivity image of Hurricane Dolly (2008) is shown in Fig. 1. Shortly after the time of this radar image, as Dolly was approaching the Texas coast, the National Hurricane Center best-track intensity estimate was 80 kt (41.2 m s^{-1}) and 976 mb (valid at 1200 UTC 23 July 2008). Note the wavenumber-4 pattern in the eyewall and the appearance of both straight line segments and mesovortices. Because of the high correlation of radar reflectivity and vorticity (e.g., Fig. 1 of Kossin et al. 2000), it can reasonably be concluded that the radar image of Dolly has captured the barotropic instability of a thin vorticity ring. In this regard it should be noted that although the Rayleigh necessary condition for dynamic instability is satisfied for all rings, not all rings are unstable. In particular, thick rings, which may be analogous to annular hurricanes (Knaff et al. 2003), are usually stable to exponentially growing perturbations.

These PV mixing episodes are thought to be an important internal mechanism governing hurricane intensity change on time scales of 1 to 24 h. Mixing of PV from the eyewall into the eye changes the tangential wind profile inside the radius of maximum wind (RMW) from U-shaped ($\partial^2 v/\partial r^2 > 0$) to Rankine-like ($\partial^2 v/\partial r^2 \approx 0$). Although it might be expected that the maximum tangential velocity would decrease as the PV is radially broadened, the mixing of PV into the eye causes the v^2/r term in the gradient wind equation to become very large, which supports a decrease in central pressure. This dual nature of PV mixing has recently been studied using a forced barotropic model (Rozoff et al. 2009). In addition, eye mesovortices that sometimes form are thought to be important factors governing intensity

change because they may serve as efficient transporters of high-moist-entropy air at low levels of the eye to the eyewall (Persing and Montgomery 2003; Montgomery et al. 2006; Cram et al. 2007), allowing the hurricane to exceed its axisymmetric energetically based maximum potential intensity (Emanuel 1986, 1988).

To obtain insight into the basic dynamics of this problem, SM99 performed a linear stability analysis for hurricane-like rings of enhanced vorticity. By defining a ring thickness parameter (ratio of the inner and outer radii) and a ring hollowness parameter (ratio of the eye to the inner-core vorticity), they were able to express the exponential growth rates of disturbances of various azimuthal wavenumbers in this thickness–hollowness space. In the aggregate, they found that the fastest growth rates existed for thin, hollow rings, while slower growth rates existed for thick, filled rings. Very thick rings were found to be stable to exponentially growing perturbations of all azimuthal wavenumbers. The nonlinear evolution of a prototypical hurricane-like vorticity ring was examined to study the details of a vorticity mixing episode. In the early phase, a polygonal eyewall (multiple straight line segments) was observed; later, as high PV fluid was mixed from the eyewall to the eye, asymmetric eye contraction occurred. This confirmed that polygonal eyewalls can be attributed solely to vorticity dynamics rather than to transient inertia–gravity wave interference patterns (Lewis and Hawkins 1982). After 24 h, the initial vorticity field was essentially redistributed into a nearly symmetric monopole. In general, it is not possible to accurately predict such end states analytically (i.e., without numerically simulating the nonlinear advection); however, the use of vortex minimum enstrophy and maximum entropy approaches have yielded some useful insight (SM99, sections 5 and 6).

In the present work, we examine the complete life cycles of 170 different vorticity rings in a nondivergent barotropic model framework. The model experiments sample the two-dimensional parameter space using 10 different values of hollowness (hollow to nearly filled) and 17 values of ring thickness (thick to thin). These rings are indicative of vorticity structures present in a wide spectrum of real hurricanes. In the initial linear wave growth phase, the nondivergent barotropic model results are compared to the SM99 linear theory for the most unstable azimuthal mode. The unforced evolution is then allowed to progress into its fully nonlinear phase. The end states (defined at t = 48 h) are assessed and characterized for each ring. Azimuthal mean diagnostics are also presented showing the evolution of the radial pressure and tangential wind profiles for each ring to assess the relationship between PV mixing events and hurricane intensity change. Provided that the basic structure of the vorticity field can be ascertained, these results can be used as a guide for understanding vorticity redistribution in real hurricanes.

The outline of this paper is as follows. In section 2, the linear stability analysis of SM99 is briefly reviewed. The pseudospectral barotropic model and initial conditions are described in section 3. To examine the utility of the numerical model results, observations of PV mixing in hurricanes are reviewed in section 4. A comparison of the fastest-growing azimuthal mode observed in the numerical model to the linear stability analysis is provided in section 5. The end states of the unstable vortices are characterized and discussed in section 6. A discussion of the relationship between PV mixing and hurricane intensity change is presented in section 7. Finally, a summary of the results is given in section 8.

2. Review of linear stability analysis

It is well known that the sign reversal in the radial vorticity gradient in hurricanes satisfies the Rayleigh necessary condition for barotropic instability.[1] One can view the instability as originating from the interaction of two counterpropagating vortex Rossby (or PV) waves (Guinn and Schubert 1993; Montgomery and Kallenbach 1997). A Rossby wave on the inner edge of the annulus will prograde relative to the mean flow, and a Rossby wave on the outer edge will retrograde relative to the mean flow. If these waves phase-lock (i.e., have the same angular velocity), it is possible for the whole wave pattern to amplify.

A linear stability analysis of initially hollow vorticity structures was performed by SM99 (their section 2). A brief review of that work is presented here. First, the discrete vorticity model is defined as three separate regions: eye, eyewall, and environment (see also Michalke and Timme 1967; Vladimirov and Tarasov 1980; Terwey and Montgomery 2002). The corresponding basic state vorticity is defined as

$$\bar{\zeta}(r) = \begin{cases} \xi_a + \xi_b & \text{if} \quad 0 \le r < r_a \,(\text{eye}) \\ \xi_b & \text{if} \quad r_a < r < r_b \,(\text{eyewall}), \\ 0 & \text{if} \quad r_b < r < \infty \,(\text{far-field}) \end{cases} \tag{1}$$

where the constants ξ_a and ξ_b are the vorticity jumps at the radii r_a and r_b. Small-amplitude perturbations to this basic state vorticity are governed by the linearized nondivergent barotropic vorticity equation

[1] In real hurricanes, where vertical shear and baroclinicity is nontrivial, we expect the instability to be a combined barotropic–baroclinic one. See Montgomery and Shapiro (1995) for a discussion of the Charney–Stern and Fjortoft theorems applicable to baroclinic vortices.

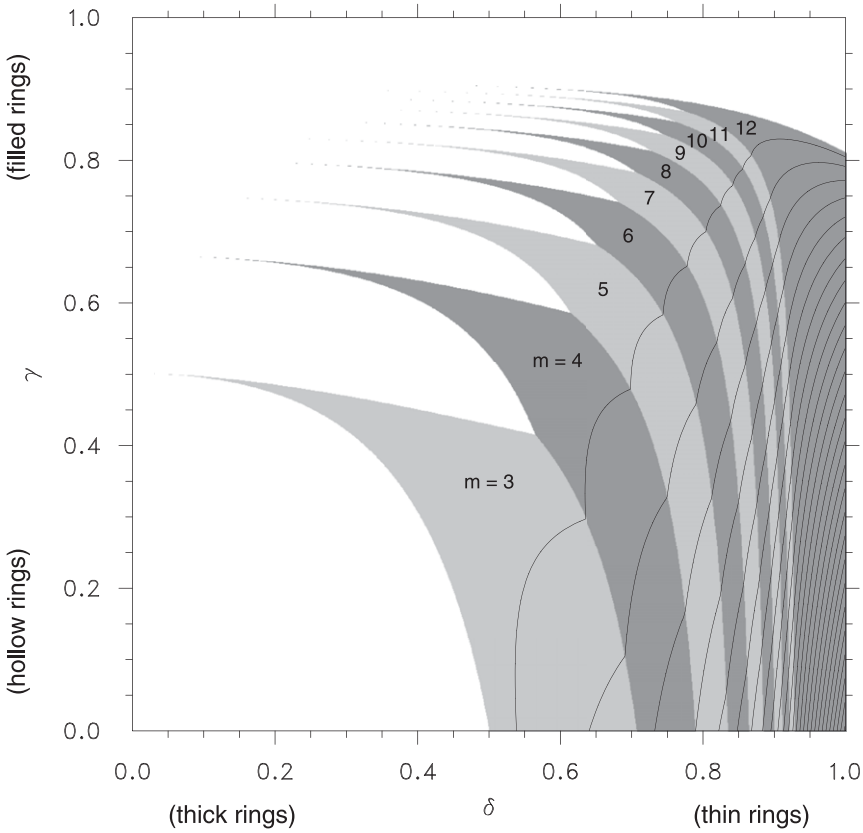

FIG. 2. Isolines of the maximum dimensionless growth rate $\nu_i/\zeta_{\rm av}$ for azimuthal wavenumbers $m = 3, 4, \ldots, 12$. Contours range from 0.1 to 2.7 (lower right), with an interval of 0.1. The shaded regions indicate the wavenumber of the maximum growth rate at each δ (abscissa) and γ (ordinate) point.

$$\left(\frac{\partial}{\partial t} + \bar{\omega}\frac{\partial}{\partial \phi}\right)\nabla^2\psi' - \frac{\partial\psi'}{r\partial\phi}\frac{d\bar{\zeta}}{dr} = 0, \qquad (2)$$

where $\bar{\omega}(r) = \bar{v}/r$ is the basic state angular velocity, $u' = -\partial\psi'/r\partial\phi$ is the perturbation radial velocity, $v' = \partial\psi'/\partial r$ is the perturbation azimuthal velocity, and $\zeta' = \nabla^2\psi'$ is the perturbation relative vorticity. By seeking solutions of the form $\psi'(r,\phi,t) = \hat{\psi}(r)e^{i(m\phi-\nu t)}$ (where m is the azimuthal wavenumber and ν is the complex frequency), (2) reduces to an ordinary differential equation for the radial structure function $\hat{\psi}(r)$. Using the $\hat{\psi}(r)$ solution in conjunction with appropriate boundary conditions, a mathematical description of the traveling vortex Rossby waves at the two vorticity jumps is obtained, along with their mutual interaction. The eigenvalue relation can be written in a physically revealing form by introducing two vortex parameters, $\delta = r_a/r_b$ and $\gamma = (\xi_a + \xi_b)/\zeta_{av}$ (where $\zeta_{av} = \xi_a\delta^2 + \xi_b$ is the average vorticity over the region $0 \le r \le r_b$). Then, the dimensionless complex frequency ν/ζ_{av} can be expressed solely in terms of the azimuthal wavenumber m, the ring thickness parameter δ, and the ring hollowness parameter γ as

$$\frac{\nu}{\zeta_{\rm av}} = \frac{1}{4}\left[m + (m-1)\gamma \pm \left(\left\{[m-(m-1)]\gamma - 2\left(\frac{1-\gamma\delta^2}{1-\delta^2}\right)\right\}^2 + 4\left(\frac{1-\gamma\delta^2}{1-\delta^2}\right)\left(\gamma - \frac{1-\gamma\delta^2}{1-\delta^2}\right)\delta^{2m}\right)^{\frac{1}{2}}\right]. \qquad (3)$$

Exponentially growing or decaying modes occur when the imaginary part of the frequency ν_i is nonzero (i.e., when the term in the square root is negative). Isolines of the dimensionless growth rate $\nu_i/\zeta_{\rm av}$ can then be drawn in the (δ, γ)-parameter space for each azimuthal wavenumber m. This set of diagrams can be collapsed into a single summary diagram by choosing the most rapidly growing wave for each point in the (δ, γ)-parameter space. This summary diagram is shown in Fig. 2. As an example of interpreting this diagram, consider a vortex defined by (δ, γ) = (0.7, 0.3). According to Fig. 2, the most unstable mode is $m = 4$; this mode grows at the rate $\nu_i/\zeta_{\rm av} \approx 0.15$. For a hurricane-like vorticity of

$\zeta_{av} = 2.0 \times 10^{-3}\ s^{-1}$, this corresponds to an *e*-folding time of 0.93 h.

The rings considered in SM99 were stable to exponentially growing modes of wavenumber $m = 1$ and $m = 2$. As shown by Terwey and Montgomery (2002), there does exist an exponentially growing $m = 2$ mode in the discrete model; however, a necessary condition for it is that $|\xi_b| < |\xi_a|$ (the eye vorticity is negative). This mode is absent from Fig. 2 because only $\gamma \geq 0$ is considered. In the analogous continuous model (6) with smooth transitions instead of vorticity jumps, exponentially growing $m = 2$ modes are also possible (SM99; Reasor et al. 2000).

Both the discrete and continuous models are stable to exponentially growing wavenumber $m = 1$ modes (Reznik and Dewar 1994). However, an algebraic $m = 1$ instability that grows as $t^{1/2}$ (Smith and Rosenbluth 1990) exists. The only requirement for this instability is a local maximum in angular velocity (Nolan and Montgomery 2000), which occurs for every vortex considered in SM99 and here. However (as will be shown), the $m = 1$ algebraically growing mode is only visible in rings that are stable to all the exponentially growing modes (thick and filled rings). The $m = 1$ instability is visible as a growing wobble of the eye (Nolan et al. 2001).

The SM99 linear analysis was generalized by Nolan and Montgomery (2002) to three-dimensional idealized hurricane-like vortices. Broadly, they found that the unstable modes were close analogs of their barotropic counterparts.

3. Pseudospectral model experiments

A nondivergent barotropic model is used for all the simulations. The model is based on one prognostic equation for the relative vorticity and a diagnostic equation for the streamfunction, from which the winds are obtained ($u = -\partial\psi/\partial y$ and $v = \partial\psi/\partial x$); that is,

$$\frac{\partial\zeta}{\partial t} + \frac{\partial(\psi,\zeta)}{\partial(x,y)} = \nu\nabla^2\zeta, \tag{4}$$

$$\zeta = \nabla^2\psi, \tag{5}$$

where ν is the kinematic viscosity. The initial condition consists of an axisymmetric vorticity ring defined by

$$\bar{\zeta}(r,0) = \begin{cases} \zeta_1 & 0 \leq r \leq r_1 \\ \zeta_1 S\left(\dfrac{r-r_1}{r_2-r_1}\right) + \zeta_2 S\left(\dfrac{r_2-r}{r_2-r_1}\right) & r_1 \leq r \leq r_2 \\ \zeta_2 & r_2 \leq r \leq r_3, \\ \zeta_2 S\left(\dfrac{r-r_3}{r_4-r_3}\right) + \zeta_3 S\left(\dfrac{r_4-r}{r_4-r_3}\right) & r_3 \leq r \leq r_4 \\ \zeta_3 & r_4 \leq r < \infty \end{cases} \tag{6}$$

where $\zeta_1, \zeta_2, \zeta_3, r_1, r_2, r_3$, and r_4 are constants and $S(s) = 1 - 3s^2 + 2s^3$ is a cubic Hermite shape function that provides smooth transition zones. The eyewall is defined as the region between r_2 and r_3, and the transition zones are defined as the regions between r_1 and r_2, and r_3 and r_4. To relate the smooth continuous model (6) to the discrete model (1), the midpoints of the smooth transition zones are used to compute the thickness parameter, so that $\delta = (r_1 + r_2) / (r_3 + r_4)$.

To initiate the instability process, a broadband perturbation (impulse) was added to the basic state vorticity (6) of the form

$$\zeta'(r,\phi,0) = \zeta_{amp}\sum_{m=1}^{12}\cos(m\phi + \phi_m) \times \begin{cases} 0 & 0 \leq r \leq r_1, \\ S\left(\dfrac{r_2-r}{r_2-r_1}\right) & r_1 \leq r \leq r_2, \\ 1 & r_2 \leq r \leq r_3, \\ S\left(\dfrac{r-r_3}{r_4-r_3}\right) & r_3 \leq r \leq r_4, \\ 0 & r_4 \leq r < \infty, \end{cases} \tag{7}$$

where $\zeta_{amp} = 1.0 \times 10^{-5}\ s^{-1}$ is the amplitude and ϕ_m is the phase of azimuthal wavenumber m. For this set of experiments, the phase angles ϕ_m were chosen to be random numbers in the range $0 \leq \phi_m \leq 2\pi$. In real hurricanes, the impulse is expected to develop from a wide spectrum of background convective motions.

A sequence of 170 numerical experiments was conducted using a pseudospectral discretization of the model. The experiments were designed to cover the thickness–hollowness (δ, γ) parameter space described above at regular intervals. The four radii (r_1, r_2, r_3, r_4) were chosen to create 17 distinct values of the thickness parameter $\delta = (r_1 + r_2) / (r_3 + r_4)$; that is, $\delta = (0.05, 0.10, \ldots, 0.85)$. This was accomplished by first setting r_3 and r_4 constant at 38 and 42 km, respectively. Then, r_1 and r_2 were varied under the constraint that $r_2 - r_1 = 4$ km to produce the desired values of δ. For example, $r_1 = 0$ km and $r_2 = 4$ km defined the $\delta = 0.05$ point, $r_1 = 2$ km and $r_2 = 6$ km defined the $\delta = 0.10$ point, and so forth. The thinnest ring was defined by $r_1 = 32$ km and $r_2 = 36$ km, corresponding to $\delta = 0.85$ and resulting in a 6-km-thick eyewall. The γ points were defined as follows: First, the inner-core average vorticity was set to $\zeta_{av} = 2.0 \times 10^{-3}$ (this value corresponds to a hurricane with maximum sustained winds of approximately 40 m s^{-1} for the radii chosen). Then, the eye vorticity ζ_1 was incremented to produce 10 values of $\gamma = \zeta_1/\zeta_{av}$; that is, $\gamma = (0.00, 0.10, \ldots, 0.90)$. The eyewall vorticity ζ_2 was then calculated by $\zeta_2 = \zeta_{av}(1 - \gamma\delta^2) / (1 - \delta^2)$. In each experiment the environmental vorticity ζ_3 was set so that the domain average vorticity would vanish.

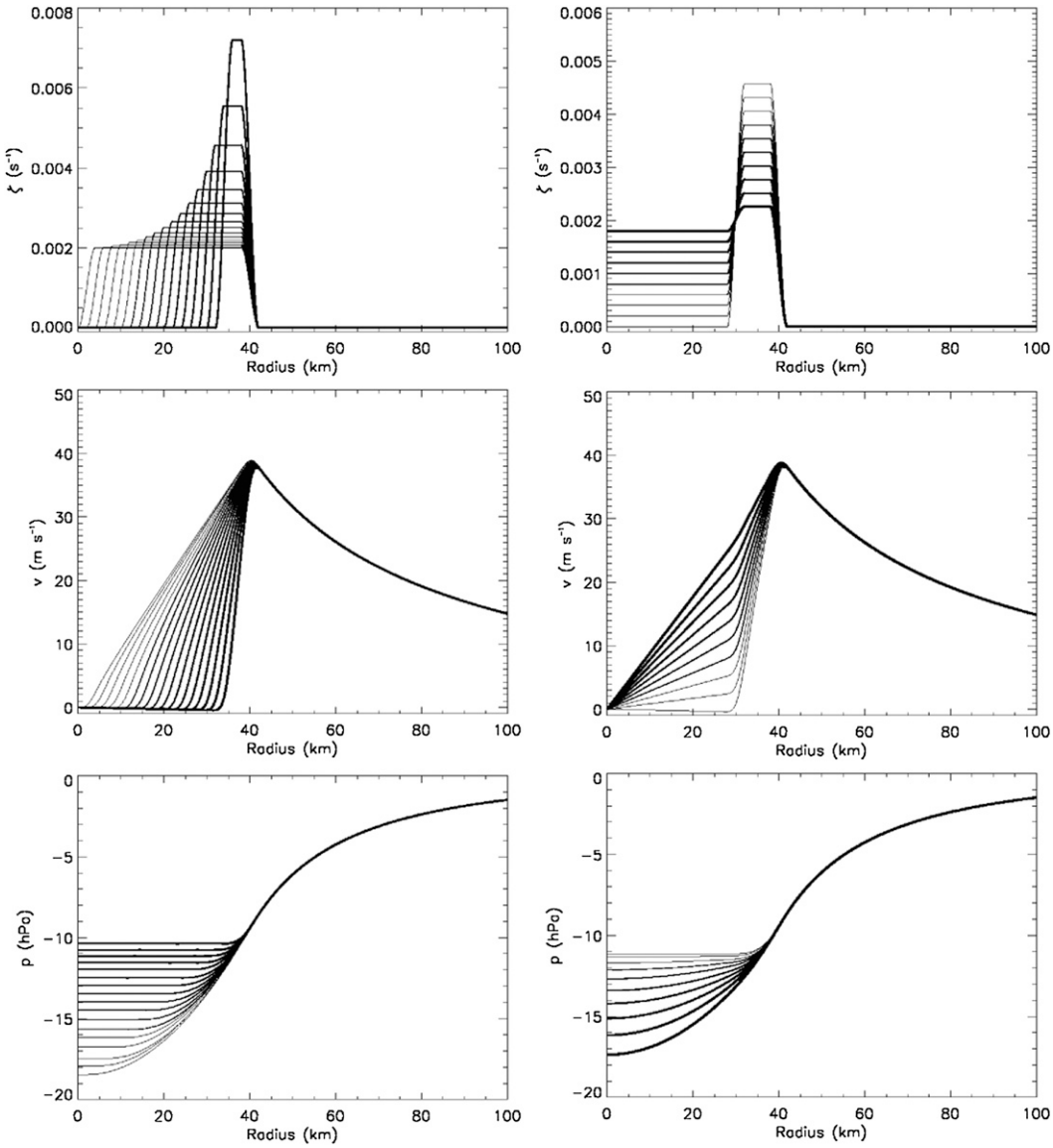

FIG. 3. Basic state initial condition of various rings. Azimuthal mean relative vorticity, azimuthal velocity, and pressure are shown for (left) $\gamma = 0.0$ and $\delta = 0.00, 0.05, \ldots, 0.85$ and (right) $\gamma = 0.0, 0.1, \ldots, 0.9$ and $\delta = 0.75$. On the left, thicker lines indicate increasing δ (rings become thinner); on the right, thicker lines indicate increasing γ (rings become more filled).

The numerical solution was obtained on a 600 km × 600 km doubly periodic domain using 512 × 512 equally spaced points. One 48-h simulation was conducted for each of the 170 points in the (δ, γ)-parameter space. After dealiasing of the quadratic advection term in (4), the number of retained Fourier modes yielded an effective resolution of 3.52 km. A standard fourth-order Runge–Kutta time scheme was used with a time step of 10 s. The diffusion coefficient on the right-hand side of (4) was set to $\nu = 25\ \mathrm{m^2\ s^{-1}}$, resulting in a ($1/e$) damping time of 3.5 h for the highest retained wavenumbers. The same random impulse (7) was added to the basic state axisymmetric vorticity field in the eyewall region for each experiment.

The initial conditions of the numerical model experiments are shown in Fig. 3. In the left panels, the mean relative vorticity, tangential velocity, and pressure anomaly are shown for the [$\gamma = 0.0$, $\delta = 0.00, 0.05, \ldots, 0.85$] rings. This illustrates how varying the ring thickness affects the three curves while holding the hollowness fixed. Similarly, the initial conditions for the [$\gamma = 0.0, 0.1, \ldots, 0.9$, $\delta = 0.75$] rings are shown in the right panels.

This illustrates how the three curves change as the hollowness parameter γ is varied while holding the thickness parameter δ fixed. In the left panel, thicker curves represent thinner rings; in the right panel, thicker curves represent more filled rings. Note that in each case only the inner-core profiles ($r < 42$ km) are changing and that the maximum tangential velocity is always the same (approximately 40 m s^{-1}). The pressure fields, displayed in the bottom panels of Fig. 3, were obtained by solving the nonlinear balance equation

$$\frac{1}{\rho}\nabla^2 p = f\nabla^2\psi - 2\left[\left(\frac{\partial^2\psi}{\partial x\partial y}\right)^2 - \frac{\partial^2\psi}{\partial x^2}\frac{\partial^2\psi}{\partial y^2}\right], \qquad (8)$$

using $f = 5 \times 10^{-5}\text{s}^{-1}$ and $\rho = 1.13$ kg m^{-3}. According to (8), in the nondivergent barotropic model the pressure immediately adjusts to the evolving wind field. In the real atmosphere and in primitive equation models, the adjustment may be accompanied by inertia–gravity wave emission, which is obviously nonexistent in the nondivergent barotropic model framework.

Two integral properties associated with (4) and (5) on a closed domain are the kinetic energy and enstrophy relations

$$\frac{d\mathcal{E}}{dt} = -2\nu\mathcal{Z} \quad \text{and} \qquad (9)$$

$$\frac{d\mathcal{Z}}{dt} = -2\nu\mathcal{P}, \qquad (10)$$

where $\mathcal{E} = \iint \frac{1}{2}\nabla\psi\cdot\nabla\psi\, dx\, dy$ is the kinetic energy, $\mathcal{Z} = \iint \frac{1}{2}\zeta^2 dx\, dy$ is the enstrophy, and $\mathcal{P} = \iint \frac{1}{2}\nabla\zeta\cdot\nabla\zeta\, dx\, dy$ is the palinstrophy. In the absence of diffusion, both kinetic energy and enstrophy are conserved. However, diffusion is necessary to damp the enstrophy cascade to high wavenumbers in a finite-resolution model. During vorticity mixing events $\mathcal{P}$ becomes very large, causing $\mathcal{Z}$ to decrease. As $\mathcal{Z}$ becomes smaller, $\mathcal{E}$ decreases at a slower rate. Thus, enstrophy is selectively decayed over energy.

4. Observations of vorticity mixing

Observations of the intricate details of inner-core vorticity mixing in hurricanes have been sparse. Dense spatial and temporal measurements of the horizontal velocity are necessary. As a result, most insight into inner-core vorticity mixing has been obtained through diagnostics of the output of numerical model simulations. The most complete observational study of internal vorticity mixing in hurricanes is Kossin and Eastin (2001). Using radial flight leg data from a number of hurricanes, they found two distinct regimes of the kinematic and thermodynamic structure of the hurricane eye and eyewall. The first regime was characterized by an annular radial profile of relative vorticity with a maximum in the eyewall region, whereas the second regime was marked by a nearly monotonic profile with a maximum in the eye. These two regimes are illustrated in Fig. 4. They showed that typically there is a transition from the first regime to the second regime on a time scale of 12–24 h. Before the transition, the eye is dry; after the transition, the eye becomes moister at low levels.

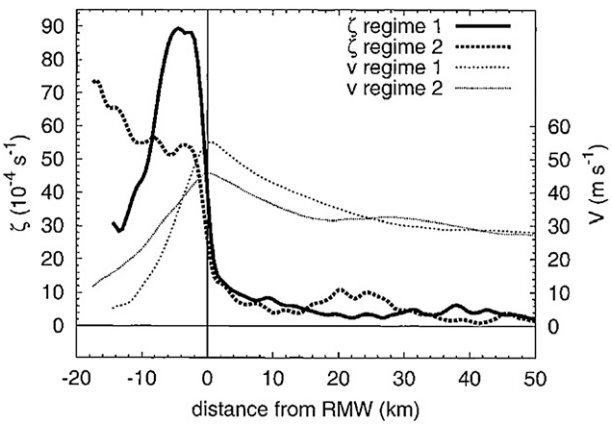

FIG. 4. Averaged relative vorticity ζ and tangential velocity v radial profiles at 850 mb in Hurricane Diana (1984). Plots are shown with respect to the radius of maximum wind. Reproduced from Kossin and Eastin (2001).

To see how these observations fit into our two-dimensional parameter space, we now estimate the values of δ and γ implied by Fig. 4. We first assume axisymmetry and look at the plot with respect to the storm center rather with respect to the radius of maximum wind. For regime 1 (solid curve), $r_a \approx 13$ km and $r_b \approx 20$ km, yielding $\delta = r_a/r_b = 0.65$. To determine γ, the average inner-core and eye vorticity (ζ_{av} and $\xi_a + \xi_b$ respectively) must be obtained. In the inner core ($r <$ RMW), $\zeta_{\text{av}} \approx 50 \times 10^{-4}\,\text{s}^{-1}$ and $\xi_a + \xi_b = 30 \times 10^{-4}\,\text{s}^{-1}$. Using these values, $\gamma = (\xi_a + \xi_b)/\xi_{\text{av}} \approx 0.6$. Summarizing, the inner-core vorticity profile of Hurricane Diana (1984) in regime 1 at this time can be characterized by $(\delta, \gamma) \approx (0.65, 0.60)$. As will be shown in the next sections, dynamic instability of such a ring in a nondivergent barotropic model would support a wavenumber-5 breakdown and slow mixing into a monopole. Note that at a later time, Diana has an approximately monopolar vorticity radial profile (regime 2). Note also that the peak tangential wind decreases in the transition from regime 1 to regime 2, which will also be shown to occur in the nondivergent barotropic model (section 7).

γ	0.05	0.10	0.15	0.20	0.25	0.30	0.35	0.40	0.45	0.50	0.55	0.60	0.65	0.70	0.75	0.80	0.85
0.9	S	S	S	S	S	S	S	S	S	S	S	S	S	W13	W14	W15	W16
0.8	S	S	S	S	S	S	S	S	S	S	S	W7	W8	W8	W8	W9	W11
0.7	S	S	S	S	S	S	S	S	S	W5	W5	W5	W6	W6	W7	W7	W9
0.6	S	S	S	S	S	S	S	S	W4	W4	W4	W4	W5	W5	W6	W6	W8
0.5	S	S	S	S	S	S	S	S	S	S	W4	W4	W4	W5	W5	W6	W7
0.4	S	S	S	S	S	S	W3	W3	W3	W3	W3	W4	W4	W4	W5	W5	W7
0.3	S	S	S	S	S	S	S	S	W3	W3	W3	W3	W4	W4	W4	W5	W6
0.2	S	S	S	S	S	S	S	S	W3	W3	W3	W3	W3	W4	W4	W5	W6
0.1	S	S	S	S	S	S	S	S	S	W3	W3	W3	W3	W4	W4	W5	W6
0	S	S	S	S	S	S	S	S	S	W3	W3	W3	W3	W3	W4	W5	W6

(filled rings) (hollow rings) (thick rings) δ (thin rings)

γ	0.05	0.10	0.15	0.20	0.25	0.30	0.35	0.40	0.45	0.50	0.55	0.60	0.65	0.70	0.75	0.80	0.85
0.9	W1	W1	W1	W1	W1	W1	W1	W2	W2	W2	W2	W2	U	U	U	U	U
0.8	W1	W1	W1	W1	W1	W1	W1	W1	W2	W2	W2	W2	U	U	U	U	U
0.7	W1	W1	W1	W1	W1	W1	W1	W1	W1	W2	W5	W6	W6	W7	W7	W8	W10
0.6	W1	W1	W1	W1	W1	W1	W1	W1	W1	W4	W5	W5	W5	W6	W6	W7	W9
0.5	W1	W1	W1	W1	W1	W1	W1	W1	W1	W4	W4	W4	W5	W5	W5	W6	W8
0.4	W1	W1	W1	W1	W1	W1	W3	W3	W3	W3	W4	W4	W4	W5	W5	W6	W7
0.3	W1	W1	W1	W1	W1	W1	W3	W3	W3	W3	W3	W4	W4	W4	W5	W5	W7
0.2	W1	W1	W1	W1	W1	W1	W1	W3	W3	W3	W3	W3	W4	W4	W5	W5	W6
0.1	W1	W1	W1	W1	W1	W1	W1	W3	W3	W3	W3	W3	W3	W4	W4	W5	W6
0	W1	W1	W1	W1	W1	W1	W1	W1	W3	W3	W3	W3	W3	W4	W4	W5	W6

(filled rings) (hollow rings) (thick rings) δ (thin rings)

FIG. 5. (top) Fastest-growing wavenumber m (Wm) instability at the discrete δ (abscissa) and γ (ordinate) points using the linear stability analysis of SM99; (bottom) the observed values from the pseudospectral model. In the top, the "S" denotes that the vortex was stable to exponentially growing perturbations of all azimuthal wavenumbers. The "U" in the bottom panel signifies that the initial wavenumber of the instability was "undetermined" (i.e., it could not be easily determined by visual inspection of the model output).

5. Comparison of the fastest-growing azimuthal mode

The fastest-growing mode at each (δ, γ) point was determined from the output of the pseudospectral model and compared to the linear stability analysis. Because the initial broadband perturbation, given in (7), assigns the same amplitude to wavenumbers 1–12, the initial instability that emerges in the numerical model is the fastest-growing mode (largest dimensionless growth rate). The mode with the maximum dimensionless growth rate is shown in Fig. 5 at each of the discrete (δ, γ) points for both (top) the exact linear solution and (bottom) the observed output from the pseudospectral model. In the limit of very fine resolution in (δ, γ) space, the top panel of Fig. 5 would reduce to the shaded regions of Fig. 2. However, the fastest-growing mode is shown at the coarser (δ, γ) points in Fig. 5 to allow for a direct comparison with the numerical model (bottom panel). It is clear that when $\delta < 0.5$ the rings are usually stable to exponentially growing modes. Thicker rings are found to be more prone to lower wavenumber growth, whereas thinner rings are more prone to higher wavenumber growth. As the rings become more filled, there is a tendency for the disturbance instability to be at a higher wavenumber.

In comparing the numerical results of the pseudospectral model to the linear results of SM99 (Fig. 5, top and bottom), it is found that the SM99 linear stability analysis is a good guide to the nonlinear model behavior in the early stages of the evolution. The (δ, γ) structure of the most unstable wavenumber is similar for W3, W4, . . . , W9. There are two main differences. The first and most obvious is the W1 and W2 features observed in the numerical model that are not present in the linear stability analysis. The W1 feature is the algebraically

TABLE 1. End state definitions.

Identifier	Name	Description
TO	Trochoidal oscillation	Trochoidal oscillation due to the $m = 1$ instability
MP	Monopole	Monotonically decreasing vorticity from center
SP	Slow monopole	Same as monopole but takes longer (48 h $\leq t \leq$ 72 h)
MV	Mesovortices	Two or more mesovortices exist for $\Delta t \geq 15$ h
EE	Elliptical eyewall	Elliptically shaped eyewall
PE	Polygonal eyewall	Polygonal eyewall with straight line segments

growing instability that is not present in the linear stability analysis because of the assumed form of solution. The W2 feature is not present in the linear stability analysis because it is nonexistent in the discrete three-region model with $\gamma > 0$. The analogous continuous three-region model, on the other hand, does support this instability. It is not clear whether the W2 pattern is a result of an exponential instability (Nolan and Farrell 1999; Reasor et al. 2000), a side effect of the large area of negative vorticity, or is a by-product of nonlinear breakdown of the vorticity ring. In some of these cases, the fastest-growing mode appears to be at a higher wavenumber, but then either a secondary instability or nonlinear interactions cause it to slowly evolve into an ellipse. The second difference is that for a given ring thickness in the unstable regime, the numerical model tends to produce a slightly higher wavenumber than expected from linear theory. As an example of this, at the $(\delta, \gamma) = (0.60, 0.30)$ point the fastest-growing mode in the numerical model is wavenumber $m = 4$, whereas the linear stability analysis predicts the fastest-growing mode to be wavenumber $m = 3$. This difference is probably due to the inclusion of the 4-km-thick transition zones between the eye and eyewall and between the eyewall and environment in the numerical simulations. These transition zones were necessary to minimize the Gibbs phenomena in the pseudospectral model. The width was chosen to be as small as possible considering the model horizontal resolution, so the continuous profiles are very similar to the discrete profiles. Although the average eyewall vorticity in each case is the same, these transition zones effectively make the region of peak vorticity in the experimental rings 4 km thinner than the linear theory rings. To illustrate this, take the following example. The $(\delta = 0.70, \gamma)$ points correspond to rings with $r_1 = 26$ km, $r_2 = 30$ km, $r_3 = 38$ km, and $r_4 = 42$ km that are filled to various degrees. The same δ value would yield jump radii (r_a and r_b) from the linear theory of $r_a = 28$ km and $r_b = 40$ km. Thus, for this set of δ values, the numerical model sees a peak vorticity region (minus the smooth transitions) that is $r_3 - r_2 = 8$ km thick, whereas in the linear stability analysis the region would be $r_b - r_a = 12$ km thick. This is the primary reason that the pseudospectral model produces a higher wavenumber instability for a given δ value, and it is noticeably more pronounced for thicker rings (essentially, the top and bottom panels of Fig. 5 cannot be viewed exactly as a one-to-one comparison for the δ points).

Other factors that may contribute weakly to the observed differences are the model horizontal resolution, diffusion (not present in the inviscid vortex used in the linear stability analysis), and periodic boundary conditions. The horizontal resolution (3.52 km) is a little coarse to resolve the early disturbance growth of the thinnest rings ($\delta = 0.85$) but should be sufficient for all other rings. The inclusion of explicit diffusion ($25\ \mathrm{m^2\ s^{-1}}$) in the numerical model may have some effect on the initial wavenumber instability, but it is likely to be minor because the $(1/e)$ damping time is 3.5 h for the smallest resolvable scales. Finally, it is possible that the periodicity that exists on a square domain could induce a nonphysical $m = 4$ mode, which would tend to broaden the areal extent of the W4 region in (δ, γ) space as compared to theory. However, examining Fig. 4, this does not appear to occur. Hence, the domain size of 600 km $\times$ 600 km is large enough that the periodic boundary conditions do not appear to influence the solution to any appreciable degree. Additionally, the wide spectrum of the initial perturbations does not favor the growth of any particular mode.

6. End states after nonlinear mixing

The end states for each of the 170 experiments were determined. Generally, the end states were defined as the stable vorticity structure that existed at $t = 48$ h; however, in some cases additional information during the life cycle was included. The purpose of characterizing these end states is to provide a guide for assessing the most probable vorticity redistribution in the short term (less than 48 h), given the known axisymmetric characteristics of the initial vorticity ring.

The list of end state classifications is shown in Table 1. The monopole (MP) classification denotes that at $t = 48$ h an approximately axisymmetric, monotonically decreasing vorticity structure has been established. The slow

γ	0.05	0.10	0.15	0.20	0.25	0.30	0.35	0.40	0.45	0.50	0.55	0.60	0.65	0.70	0.75	0.80	0.85
0.9 (filled rings)	TO	TO	TO	TO	TO	TO	TO	EE	EE	EE	EE	EE	SP	SP	SP	SP	SP
0.8	TO	TO	TO	TO	TO	TO	TO	TO	EE	EE	EE	EE	SP	SP	SP	SP	SP
0.7	TO	TO	TO	TO	TO	TO	TO	TO	TO	EE	EE	SP	SP	SP	SP	SP	MP
0.6	TO	TO	TO	TO	TO	TO	TO	TO	TO	EE	EE	EE	SP	SP	SP	MP	MP
0.5	TO	TO	TO	TO	TO	TO	TO	TO	TO	PE	PE	SP	SP	MP	MP	MP	MP
0.4	TO	TO	TO	TO	TO	TO	PE	PE	PE	PE	SP	SP	SP	MP	MP	MP	MV
0.3	TO	TO	TO	TO	TO	TO	PE	SP	SP	SP	SP	MP	MP	MP	MP	MP	MV
0.2	TO	TO	TO	TO	TO	TO	TO	PE	SP	SP	SP	SP	MP	MP	MP	MP	MV
0.1	TO	TO	TO	TO	TO	TO	TO	PE	SP	SP	SP	SP	MP	MP	MP	MP	MV
0 (hollow rings)	TO	TO	TO	TO	TO	TO	TO	TO	SP	SP	SP	MP	MP	MP	MP	MP	MV

(thick rings) δ (thin rings)

FIG. 6. End states (t = 48 h) observed in the pseudospectral model after nonlinear vorticity mixing at the discrete δ (abscissa) and γ (ordinate) points.

monopole (SP) classification denotes that at t = 48 h a monopole did not yet exist, but the trend was such that if the model were run longer (in most cases, less than t = 72 h) a monopole would form. In these cases, the disturbance exponential growth rates are smaller (see Fig. 2) and therefore the model was not run long enough to capture the full axisymmetrization process. The mesovortices (MV) classification denotes that two or more local vorticity centers persisted for at least 15 h during the unforced evolution of the ring. With the exception of the (δ, γ) = (0.85, 0.10) ring (in which a stable configuration of four mesovortices existed at t = 48 h; Fig. 8, left panel), the mesovortices merged into a monopole by t = 48 h. The elliptical eyewall (EE) classification denotes an end state involving an ellipse of high vorticity. The polygonal eyewall (PE) classification denotes an end state involving an eyewall with multiple straight line segments. The shape of the polygon was found to be the same shape as the initial exponentially growing mode. Note that many of the rings with an MP or SP end state exhibited polygonal eyewalls during their evolution to a monopole (see Fig. 7). Finally, the trochoidal oscillation (TO) classification signifies that the end state is more or less identical to the initial state, with the exception of the diffusive weakening of the gradients and the trochoidal wobble of the eye due to the m = 1 algebraic instability.

The actual end states observed at t = 48 h for each (δ, γ) point are shown in Fig. 6. For very thin and hollow rings (δ = 0.85), there is a strong tendency to produce multiple persistent, long-lived mesovortices. In the unforced experiments of Kossin and Schubert (2001), mesovortices similar to these had significant meso-low pressure areas (as much as 50 mb lower than the environment), and this barotropic breakdown was therefore hypothesized to precede a rapid fall in central pressure. Examining the γ = 0 row, we see that for moderately thin hollow rings ($0.60 \leq \delta \leq 0.80$), the mostly likely end states are monopoles (MP); for thicker hollow rings ($0.45 \leq \delta \leq 0.55$), the tendency is for slow monopoles (SP); and for thick, hollow rings ($\delta \leq 0.40$), the end states are generally trochoidal oscillations (TO). For a given δ value, as the eye becomes more filled (increasing γ) there is a tendency for the mixing to a monopole to take longer (more like an SP), and it is less likely to have persistent mesovortices. For moderately thin rings ($0.45 \leq \delta \leq 0.75$) with nearly filled cores ($\gamma \geq 0.60$), there is a tendency for an end state of an elliptical eyewall (EE). This tendency is probably the result of either a slower growing wavenumber $m = 2$ exponential mode or nonlinear effects. For a few moderately filled thick rings there was a tendency for polygonal eyewalls (PE) to exist at t = 48 h. In these cases, the growth rates of the initial wavenumber m = 3 and 4 instabilities were so small that the low-vorticity eye could not be expelled or mixed out, and the resulting structure was an polygonal eyewall of the same character as the initial instability.

The complete life cycles of some unstable rings are shown in Figs. 7, 8, and 9 . The left panel of Fig. 7 depicts the evolution of the (δ, γ) = (0.75, 0.20) ring. The initial instability is m = 5 (although close to m = 4), and the end state is a monopole. The right panel of Fig. 7 depicts the evolution of the (δ, γ) = (0.50, 0.20) ring. The initial instability is m = 3, and the end state is a slow monopole. If the model were run slightly longer, the vorticity mixing process would be complete and the low-vorticity eye would be expelled. Figure 8 (left panel) depicts the evolution of the (δ, γ) = (0.55, 0.80) ring. The initial instability is m = 2, and the end state is an elliptical eyewall. Figure 8 (right panel) depicts the evolution of

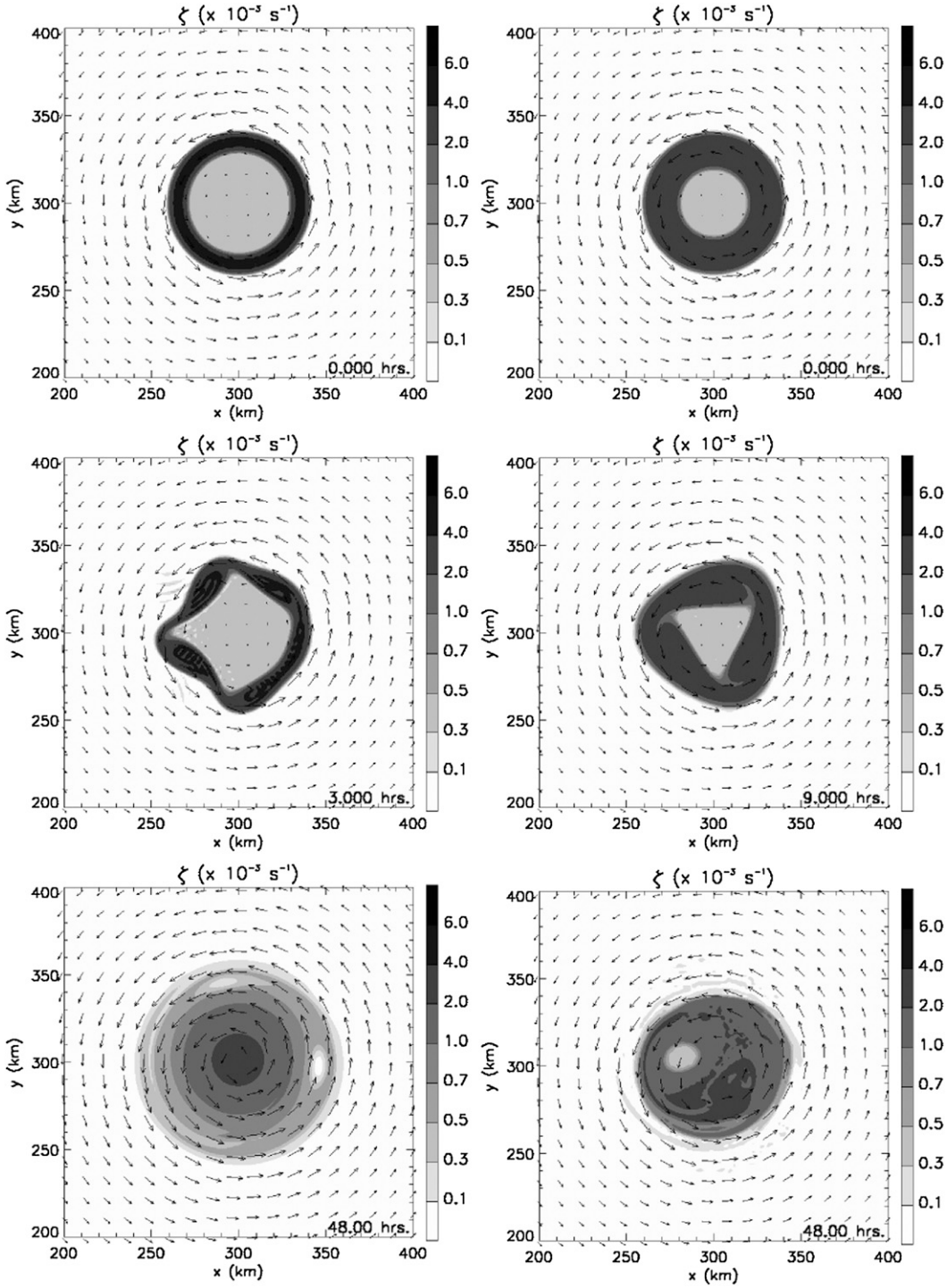

FIG. 7. The evolution of the (left) $(\delta, \gamma) = (0.75, 0.20)$ and (right) $(\delta, \gamma) = (0.50, 0.20)$ rings. The end states are MP and SP, respectively.

the $(\delta, \gamma) = (0.50, 0.50)$ ring. The initial instability is $m = 4$, and the end state is a square, polygonal eyewall. Figure 9 (left panel) depicts the evolution of the $(\delta, \gamma) = (0.85, 0.10)$ ring. The initial instability is $m = 6$, and the end state is a stable (nonmerging) pattern of four mesovortices. Figure 9 (right panel) depicts the evolution of the $(\delta, \gamma) = (0.25, 0.70)$ ring. The initial instability is $m = 1$, and the end state is a stable ring with a wobbling eye.

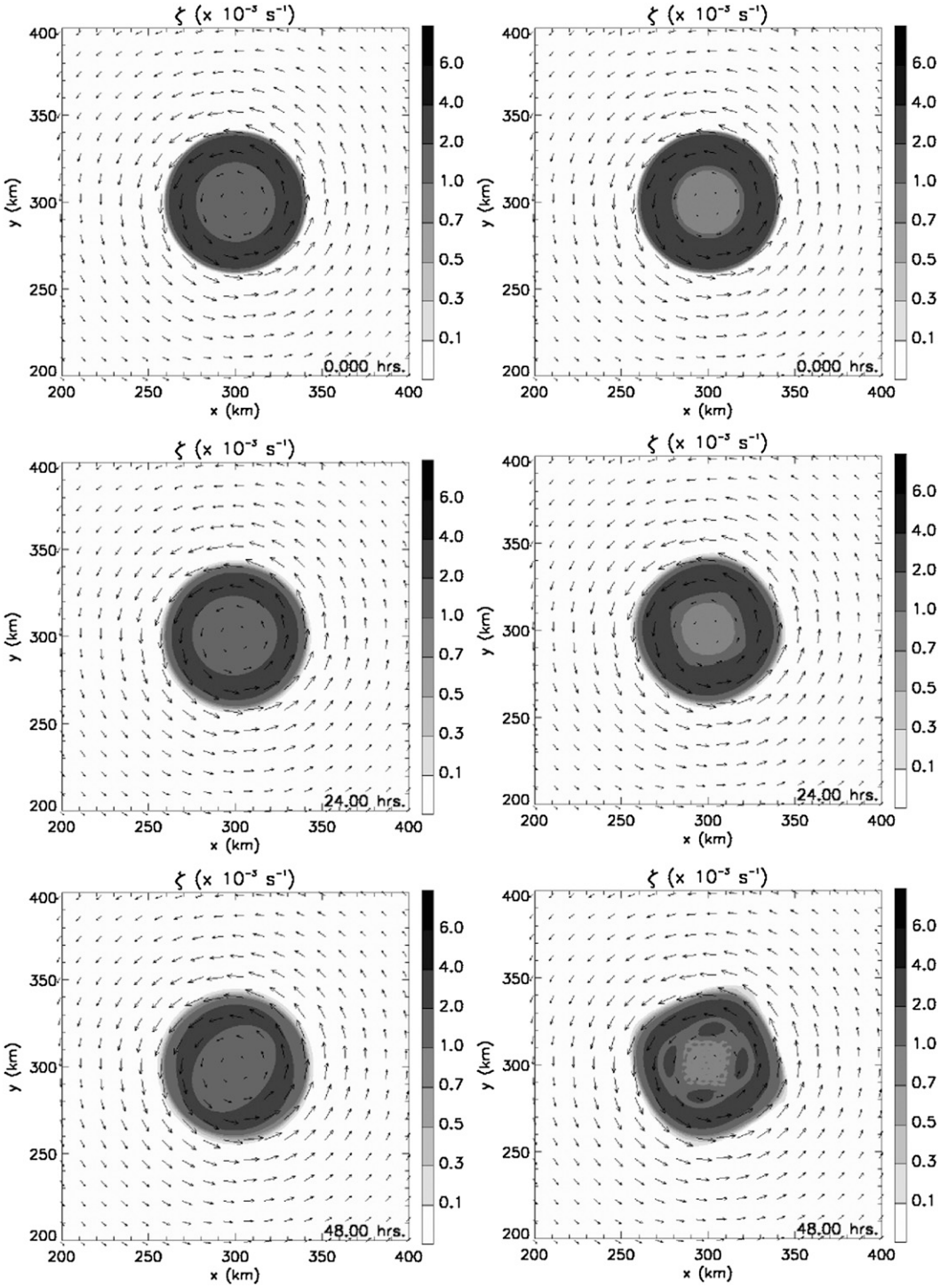

FIG. 8. The evolution of the (left) $(\delta, \gamma) = (0.55, 0.80)$ and (right) $(\delta, \gamma) = (0.50, 0.50)$ rings. The end states are EE and PE, respectively.

The evolution of the normalized enstrophy $\mathcal{Z}(t)/\mathcal{Z}(0)$ for each of the above rings is shown in Fig. 10. For the TO, EE, and PE classifications, the enstrophy decay was gradual and small. For the SP classification, the enstrophy decay was gradual and slightly larger. For the MP and MV classifications, the enstrophy decay was rapid and large. Also shown in Fig. 10 is an additional MV case, with $(\delta, \gamma) = (0.85, 0.00)$. In this

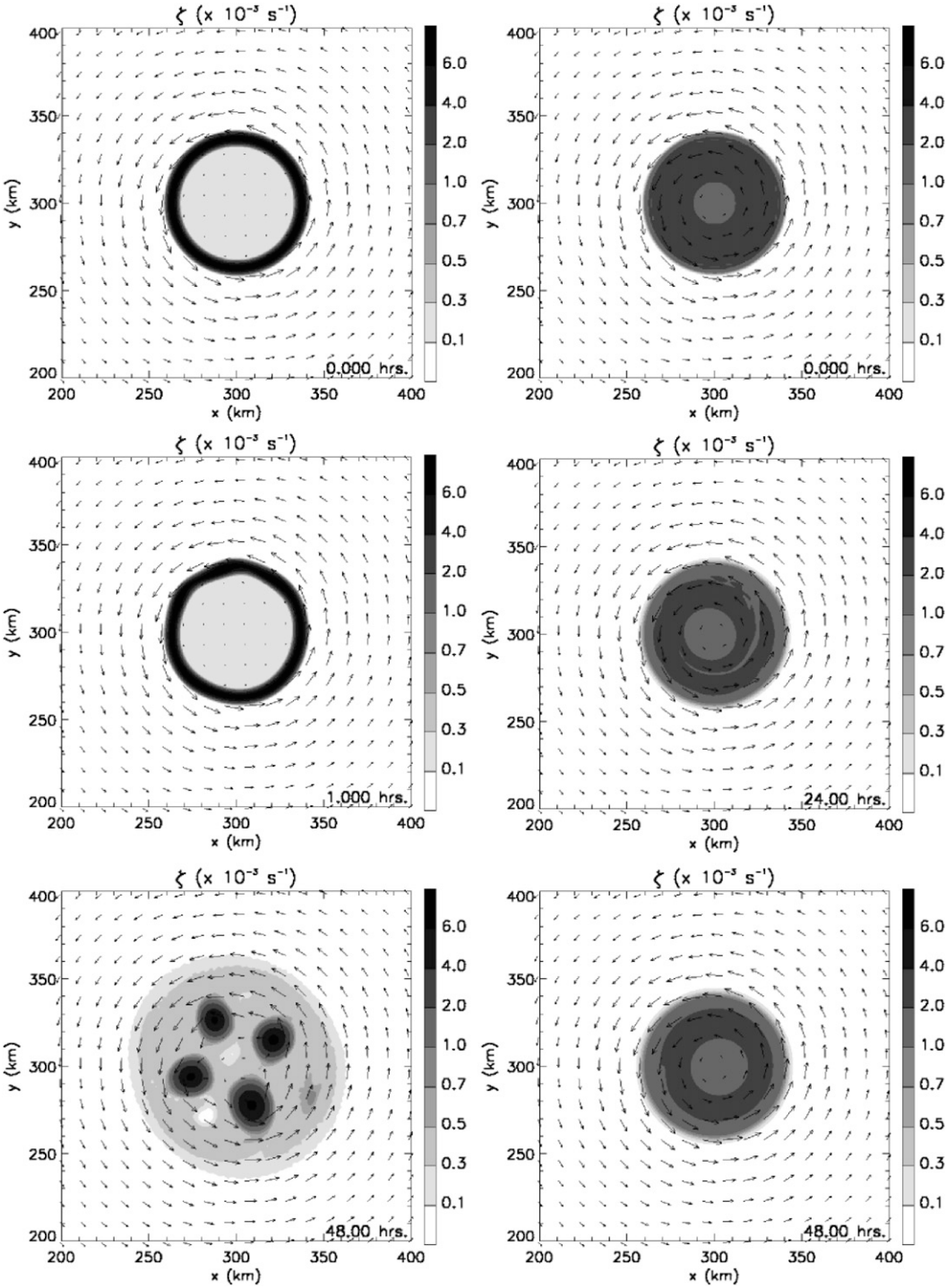

FIG. 9. The evolution of the (left) $(\delta, \gamma) = (0.85, 0.10)$ and (right) $(\delta, \gamma) = (0.25, 0.70)$ rings. The end states are MV and TO, respectively.

case, a stair-step pattern was observed in $\mathcal{Z}(t)/\mathcal{Z}(0)$, a behavior associated with mesovortex mergers. In the other MV case, this stair-step pattern was not observed because the four mesovortices that formed during the initial ring breakdown did not undergo any subsequent mergers. These results are broadly consistent with vorticity ring rearrangement study of Wang (2002).

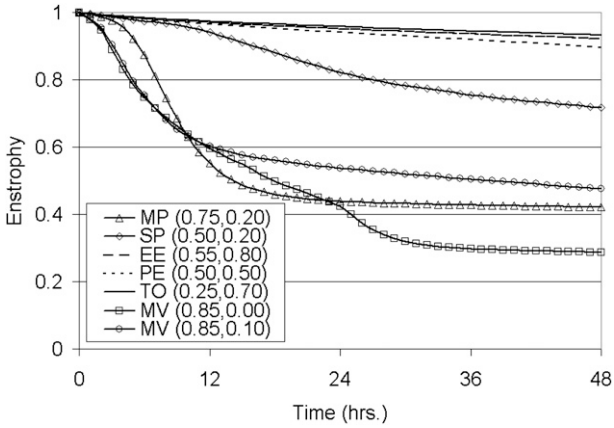

FIG. 10. Evolution of the enstrophy $Z(t)/Z(0)$ for the rings in Figs. 7–9. An additional MV curve is plotted for the $(\delta, \gamma) = (0.85, 0.00)$ ring.

7. PV mixing and hurricane intensity change

What is the relationship between inner-core PV mixing and hurricane intensity change? A complete answer to this question would require both observational analysis and a comprehensive study of forced (with diabatic heating effects) and unforced simulations using a hierarchy of numerical models: the nondivergent barotropic model, the shallow water model, the quasi-static primitive equation model, and the full-physics nonhydrostatic model. In this section, we examine the relationship between PV mixing and intensity change in the unforced nondivergent barotropic context.

In Fig. 11, the azimuthal mean vorticity, tangential velocity, and central pressure at $t = 0$ h (solid curve) and $t = 48$ h (dashed curve) are shown for the evolution of two rings: $(\delta, \gamma) = (0.7, 0.7)$ on the left and $(\delta, \gamma) = (0.85, 0.0)$ on the right. The end states are SP and MP, respectively. In the left panel it can be seen that the azimuthal mean relative vorticity is not yet monotonic, although the mixing is proceeding such that a monopole would form later. During its evolution both the peak tangential velocity and central pressure decreased slightly ($\Delta\bar{v}_{\max} = -3.9\,\mathrm{m\,s^{-1}}$ and $\Delta p_{\min} = -0.8$ hPa). In the right panel, the annulus of vorticity was redistributed to a monopole, causing the radius of maximum wind to contract approximately 25 km in 48 h. Both the tangential velocity and central pressure decreased significantly ($\Delta\bar{v}_{\max} = -7.7\,\mathrm{m\,s^{-1}}$ and $\Delta p_{\min} = -14.4$ hpa) during this period.

The changes in central pressure and maximum azimuthal mean tangential velocity for each ring examined in this study are shown in Fig. 12. In the top panel, the change in central pressure is shown, with light gray denoting a pressure change of $-5 \le \Delta p_{\min} < 0$ hPa and dark gray denoting a pressure change of $\Delta p_{\min} < -5$ hPa. In the bottom panel the changes in maximum tangential velocity are shown with light gray denoting a change of $-7 \le \Delta\bar{v}_{\max} < -3\,\mathrm{m\,s^{-1}}$ and dark gray denoting a change of $\Delta\bar{v}_{\max} < -7\,\mathrm{m\,s^{-1}}$. The main conclusion from this figure is that for all rings that underwent vorticity mixing episodes, both the tangential velocity and central pressure decreased. The decreases were most pronounced for thin, hollow rings that mixed to a monopole or mesovortices that persisted and then merged into a monopole (cf. Kossin and Schubert 2001). Note that because the $(\delta, \gamma) = (0.85, 0.10)$ ring had an end state of four mesovortices, the central pressure fall was weak; however, lower pressure anomalies were associated with each mesovortex.

At first glance, the simultaneous lowering of the central pressure and peak tangential velocity may appear to be unrealistic. Indeed, empirical wind–pressure relationships [see the reexamination by Knaff and Zehr (2007)] indicate that if the peak tangential velocity increases, the central pressure should decrease and vice versa. These relationships are generally supported observationally. From a theoretical standpoint, however, there is no reason that a hurricane-like vortex cannot have simultaneous decreases in central pressure and maximum tangential velocity. Wind–pressure relationships generally make an approximation of the form

$$v_{\max} = C(p_{\mathrm{ref}} - p_c)^n, \tag{11}$$

where C and n are empirical constants, $v_{\max}$ is the maximum azimuthal velocity, p_{ref} is the reference pressure, and p_c is the central pressure. Such approximations may not be valid during PV mixing events. To illustrate why this is the case, we write the cyclostrophic balance equation $v^2/r = (1/\rho)(\partial p/\partial r)$ in its integral form:

$$\int_0^{r_{\mathrm{ref}}} \rho \frac{v^2}{r} dr = p_{\mathrm{ref}} - p_c, \tag{12}$$

where r_{ref} is the radius at which the pressure equals p_{ref}. Comparing the empirical relation (11) with the cyclostrophic balance relation (12), we see that (11) is justified if the integral on the left-hand side of (12) can be accurately approximated by $(v_{\max}/C)^{1/n}$ for all the $v(r)$ profiles encountered during PV mixing events. Examining the two tangential velocity profiles in Fig. 11 (middle right panel), we see that although the peak tangential velocity decreased, there exists a much larger radial region of higher winds for the dashed curve at $t = 48$ h. The pressure fall, which must account for the entire radial integral, is therefore larger in this case even though the peak winds decreased. This occurs primarily

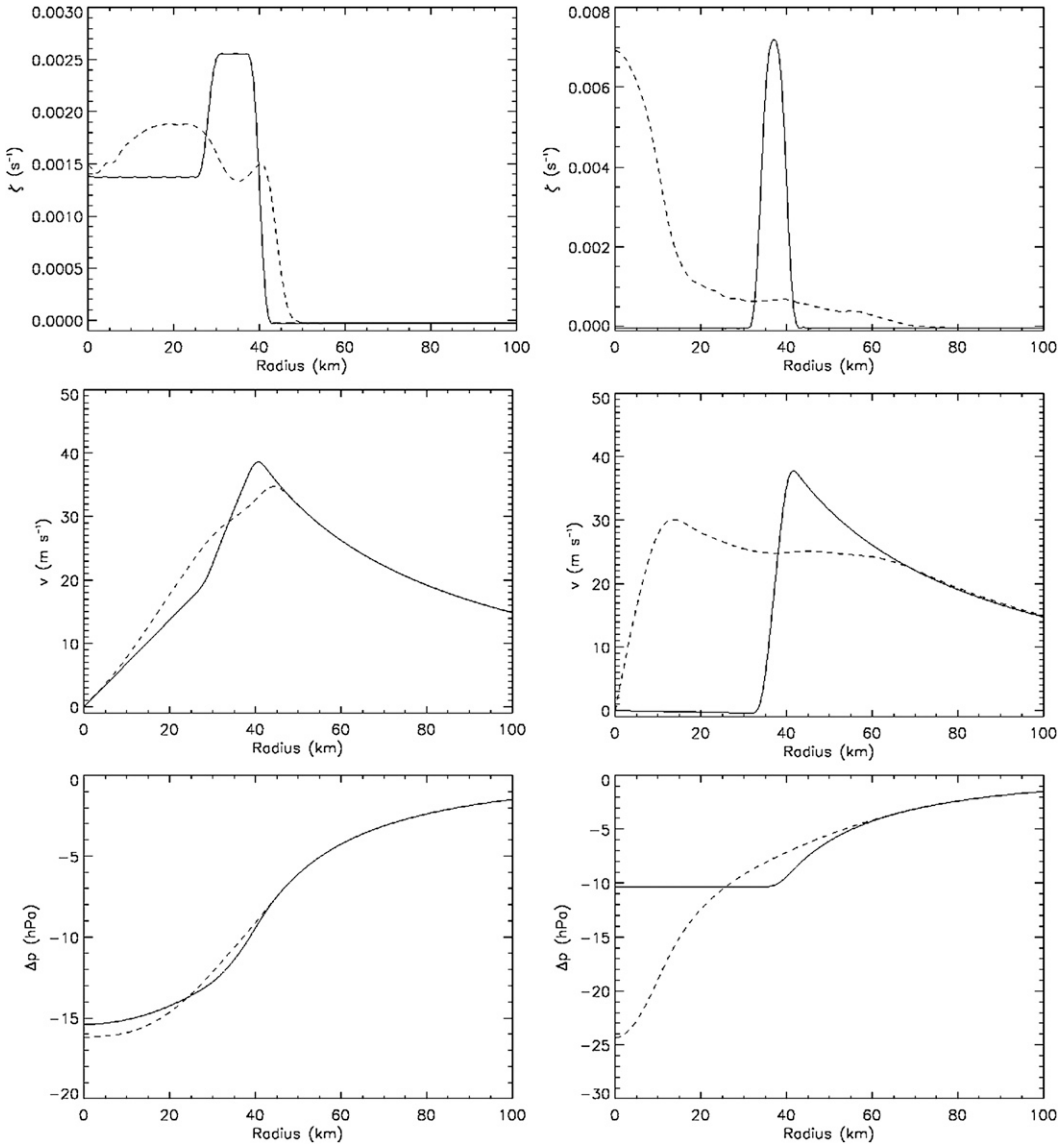

FIG. 11. The initial (t = 0 h; solid curve) and final (t = 48 h; dashed curve) azimuthal mean relative vorticity, tangential velocity, and pressure for the (left) $(\delta, \gamma) = (0.70, 0.70)$ and (right) $(\delta, \gamma) = (0.85, 0.00)$ rings. The end states of the two rings are SP and MP, respectively.

because the increase of angular momentum at small radii causes the v^2/r term to be large there. Empirical wind–pressure relationships usually work because most hurricanes have similar $v(r)$ profiles. However, during PV mixing events, the $v(r)$ profiles can change dramatically. For tropical cyclones that are undergoing significant eye–eyewall mixing, the approximation of the left-hand side of (12) will generally not be valid, and the use of $v_{\max}$ rather an integral measure (Powell and Reinhold 2007; Maclay et al. 2008) to describe hurricane intensity will not be as accurate. The authors are not aware of observations showing that a hurricane can simultaneously lower its central pressure and reduce its maximum sustained winds. It would be interesting to examine aircraft reconnaissance data to see if such observations exist. It would also be useful to observationally validate our predictions that breakdowns of hollow and thin rings produce the largest pressure falls and to examine the correlation of γ with eye size.

8. Summary

The life cycles of 170 different hurricane-like potential vorticity rings, filling the parameter space of the hollowness of the core (defined by the ratio of eye to inner-core relative vorticity) and the thickness of the

Δp_{min} (hPa)

γ \ δ	0.05	0.10	0.15	0.20	0.25	0.30	0.35	0.40	0.45	0.50	0.55	0.60	0.65	0.70	0.75	0.80	0.85
0.9	0.2	0.2	0.1	0.1	0.2	0.2	0.2	0.2	0.2	0.2	0.2	0.2	0.2	0.2	0.1	0.1	0.1
0.8	0.2	0.1	0.1	0.1	0.1	0.1	0.1	0.2	0.2	0.2	0.1	0.1	0.0	-0.1	-0.3	-0.5	-0.4
0.7	0.1	0.1	0.1	0.1	0.1	0.1	0.1	0.1	0.1	0.1	0.1	-0.2	-0.4	-0.8	-0.8	-0.9	-2.1
0.6	0.1	0.1	0.1	0.1	0.1	0.1	0.1	0.1	0.1	0.1	0.1	-0.2	-0.9	-0.5	-2.1	-3.0	-3.4
0.5	0.1	0.1	0.1	0.1	0.1	0.1	0.1	0.1	0.1	0.0	-0.5	-0.6	-1.2	-3.1	-3.7	-4.4	-5.0
0.4	0.1	0.1	0.1	0.1	0.1	0.1	0.1	0.1	0.1	0.1	-0.9	-1.6	-2.0	-4.4	-5.3	-5.8	-6.2
0.3	0.1	0.1	0.1	0.1	0.1	0.1	0.1	-0.3	-0.7	-1.2	-1.7	-3.9	-4.3	-5.7	-6.3	-6.9	-8.3
0.2	0.1	0.1	0.1	0.1	0.1	0.0	0.1	-0.3	-1.9	-2.4	-2.8	-3.4	-5.5	-6.5	-7.6	-8.0	-9.7
0.1	0.1	0.1	0.1	0.1	0.1	0.1	0.1	0.1	-1.9	-3.0	-3.0	-3.8	-6.4	-7.4	-8.3	-9.9	-1.7
0	0.1	0.1	0.1	0.1	0.1	0.2	0.2	0.2	-1.8	-3.4	-4.0	-5.8	-6.9	-8.1	-9.4	-11.2	-14.0

(filled rings) (hollow rings) (thick rings) (thin rings)

$\Delta \bar{v}_{max}$ (m s^{-1})

γ \ δ	0.05	0.10	0.15	0.20	0.25	0.30	0.35	0.40	0.45	0.50	0.55	0.60	0.65	0.70	0.75	0.80	0.85
0.9	-1.6	-1.6	-1.6	-1.6	-1.7	-1.7	-1.7	-1.7	-1.7	-1.7	-1.7	-1.7	-1.8	-1.9	-2.0	-2.1	-2.3
0.8	-1.6	-1.6	-1.6	-1.6	-1.7	-1.7	-1.7	-1.7	-1.7	-1.8	-1.8	-2.1	-2.4	-2.8	-3.2	-3.5	-3.9
0.7	-1.6	-1.6	-1.6	-1.7	-1.7	-1.7	-1.7	-1.7	-1.8	-1.8	-2.2	-2.9	-3.5	-3.9	-4.2	-5.1	-5.9
0.6	-1.6	-1.6	-1.6	-1.6	-1.7	-1.7	-1.7	-1.8	-1.8	-1.8	-2.3	-3.2	-4.8	-4.5	-6.1	-6.8	-7.2
0.5	-1.6	-1.6	-1.6	-1.7	-1.7	-1.7	-1.7	-1.8	-1.8	-2.1	-3.2	-3.8	-4.6	-6.5	-7.3	-7.6	-8.4
0.4	-1.6	-1.6	-1.6	-1.7	-1.7	-1.7	-1.8	-1.8	-1.8	-1.9	-3.1	-4.1	-4.8	-7.6	-8.7	-8.9	-9.7
0.3	-1.6	-1.6	-1.6	-1.7	-1.7	-1.7	-1.8	-2.3	-3.2	-3.6	-3.7	-7.0	-7.2	-8.9	-9.7	-10.1	-10.2
0.2	-1.6	-1.6	-1.6	-1.7	-1.7	-1.8	-1.8	-2.6	-3.2	-4.2	-4.4	-5.4	-8.3	-9.8	-10.3	-11.1	-11.5
0.1	-1.6	-1.6	-1.6	-1.7	-1.7	-1.7	-1.4	-2.0	-3.4	-4.6	-4.7	-6.2	-8.8	-10.1	-10.5	-10.7	-9.2
0	-1.6	-1.6	-1.7	-1.7	-1.7	-1.8	-1.8	-1.9	-3.4	-4.5	-5.2	-8.5	-9.3	-9.1	-9.5	-8.6	-7.7

(filled rings) (hollow rings) (thick rings) (thin rings)

FIG. 12. (top) Central pressure change (hPa) from $t = 0$ h to $t = 48$ h for each ring. Negative values (pressure drop) are shaded with $-5 \leq \Delta p_{min} \leq 0$ in light gray and $\Delta p_{min} \leq -5$ in dark gray. (bottom) Maximum tangential velocity change (m s^{-1}) from $t = 0$ h to $t = 48$ h for each ring: $-7 \leq \Delta \bar{v}_{max} \leq -3$ (light gray shading) and $\Delta \bar{v}_{max} \leq -7$ (dark gray shading).

ring (defined by the ratio of the inner and outer radii), were examined in a nondivergent barotropic model framework. In approximately half the cases the ring became exponentially unstable, causing vorticity to be mixed from the eyewall to the eye. In the early part of the life cycle, the fastest-growing exponential mode was compared to the linear stability analysis of SM99. In the later part (nonlinear mixing), the resultant end states were characterized for each ring at $t = 48$ h.

It was found that the linear stability analysis of SM99 is a good guide to the nonlinear model behavior in the exponential growth phase of the life cycle. The assumptions used in the SM99 linear stability analysis eliminated the possibility of wavenumbers $m = 1$ (algebraic) and $m = 2$ instabilities, which were both observed in the pseudospectral model results. The slowly growing wavenumber $m = 1$ instability was visible as a wobble of the eye in thick, filled rings that were stable to all other exponentially growing modes. If the vortex were moving, this wobble would be observed as a trochoidal oscillation. A wavenumber $m = 2$ pattern was observed for a few moderately thick, nearly filled rings. This was most likely due to either an exponential instability (allowed by the model's continuous vorticity profile) or nonlinear vorticity mixing. Elliptically shaped vorticity structures have been observed in hurricanes (Kuo et al. 1999; Reasor et al. 2000; Corbosiero et al. 2006) and simulated as a nonlinear interaction between a monopole and a secondary ring of enhanced vorticity (Kossin et al. 2000), but their formation dynamics are not clear in the evolution of unforced PV rings.

The most likely end state of an unstable ring is a monopole. For thick, filled rings, the relaxation to a monopole takes longer than for thin, hollow rings. For

very thin rings with relatively hollow cores, multiple long-lived (on the order of 15 h) mesovortices persisted before mixing to a monopole. For moderately thick and filled rings, the end state was an elliptical eyewall that formed because of the wavenumber $m = 2$ feature described above. For some thick and moderately filled rings, the end state was a polygonal eyewall of the same character as the initial instability.

For all rings that underwent a barotropic breakdown and vorticity mixing, both the central pressure and peak azimuthal mean tangential velocity decreased. The most dramatic pressure and tangential velocity decreases were found for thin, hollow rings that evolved to a monopole, either directly or via a number of persistent mesovortices. In a 48-h time frame, the storms that formed monopoles (on average) had a central pressure fall of 6 hPa and tangential velocity fall of 9 m s^{-1}. Weaker falls were found for slow monopoles (1 hPa and 4 m s^{-1}, respectively). Very minor changes occurred for all other rings.

In real hurricanes, diabatic effects tend to constantly produce a PV hollow tower. This hollow tower will periodically become dynamically unstable and PV will be mixed from the eyewall into the eye. Subsequently, diabatic heating will tend to regenerate the hollow tower, from which another mixing episode may occur, and so forth. In this work, we have shown which end states are most likely to result from these episodic PV mixing events for hollow towers (vorticity rings in the nondivergent barotropic context) that are filled and thin to various degrees. For strong and intensifying hurricanes that produce thin hollow towers, these results suggest another mechanism by which the central pressure can rapidly fall. Thus, PV mixing may complement the intensification process.

Finally, we have chosen a very simple framework (a nondivergent barotropic model) to study this problem. In real hurricanes, where baroclinicity and moist processes are important, these results may change to some degree. Future work should be focused on studying the relationship between inner-core PV mixing and hurricane intensity change in more complex models. A logical next step to the current work would involve similar simulations in a three-dimensional dry quasi-static primitive equation model framework, examining the life cycles of unforced (adiabatic) PV hollow towers, including the preferred isentropic layers for PV mixing.

Acknowledgments. This research was supported by NASA/TCSP Grant 04-0007-0031, NSF Grant ATM-0332197, and Colorado State University. We thank Paul Ciesielski, Christopher Davis, Richard Johnson, Kevin Mallen, Brian McNoldy, Kate Musgrave, Roger Pielke Sr., Christopher Rozoff, and Jonathan Vigh for their comments and assistance. This manuscript was improved by the helpful comments of two anonymous reviewers.

REFERENCES

Corbosiero, K. L., J. Molinari, A. R. Aiyyer, and M. L. Black, 2006: The structure and evolution of Hurricane Elena (1985). Part II: Convective asymmetries and evidence for vortex Rossby waves. *Mon. Wea. Rev.,* **134,** 3073–3091.

Cram, T. A., J. Persing, M. T. Montgomery, and S. A. Braun, 2007: A Lagrangian trajectory view on transport and mixing processes between the eye, eyewall, and environment using a high-resolution simulation of Hurricane Bonnie (1998). *J. Atmos. Sci.,* **64,** 1835–1856.

Emanuel, K., 1986: An air–sea interaction theory for tropical cyclones. Part I: Steady-state maintenance. *J. Atmos. Sci.,* **43,** 585–604.

——, 1988: The maximum intensity of hurricanes. *J. Atmos. Sci.,* **45,** 1143–1155.

Guinn, T. A., and W. H. Schubert, 1993: Hurricane spiral bands. *J. Atmos. Sci.,* **50,** 3380–3403.

Knaff, J. A., and R. Zehr, 2007: Reexamination of tropical cyclone wind–pressure relationships. *Wea. Forecasting,* **22,** 71–88.

——, J. P. Kossin, and M. DeMaria, 2003: Annular hurricanes. *Wea. Forecasting,* **18,** 204–223.

Kossin, J. P., and M. D. Eastin, 2001: Two distinct regimes in the kinematic and thermodynamic structure of the hurricane eye and eyewall. *J. Atmos. Sci.,* **58,** 1079–1090.

——, and W. H. Schubert, 2001: Mesovortices, polygonal flow patterns, and rapid pressure falls in hurricane-like vortices. *J. Atmos. Sci.,* **58,** 2196–2209.

——, and ——, 2004: Mesovortices in Hurricane Isabel. *Bull. Amer. Meteor. Soc.,* **85,** 151–153.

——, ——, and M. T. Montgomery, 2000: Unstable interactions between a hurricane's primary eyewall and a secondary ring of enhanced vorticity. *J. Atmos. Sci.,* **57,** 3893–3917.

——, B. D. McNoldy, and W. H. Schubert, 2002: Vortical swirls in hurricane eye clouds. *Mon. Wea. Rev.,* **130,** 3144–3149.

Kuo, H.-C., R. T. Williams, and J.-H. Chen, 1999: A possible mechanism for the eye rotation of Typhoon Herb. *J. Atmos. Sci.,* **56,** 1659–1673.

Lewis, B. M., and H. F. Hawkins, 1982: Polygonal eye walls and rainbands in hurricanes. *Bull. Amer. Meteor. Soc.,* **63,** 1294–1301.

Maclay, K. S., M. DeMaria, and T. H. Vonder Haar, 2008: Tropical cyclone inner-core kinetic energy evolution. *Mon. Wea. Rev.,* **136,** 4882–4898.

Michalke, A., and A. Timme, 1967: On the inviscid instability of certain two-dimensional vortex-type flow. *J. Fluid Mech.,* **29,** 647–666.

Möller, J. D., and R. K. Smith, 1994: The development of potential vorticity in a hurricane-like vortex. *Quart. J. Roy. Meteor. Soc.,* **120,** 1255–1265.

Montgomery, M. T., and L. J. Shapiro, 1995: Generalized Charney–Stern and Fjortoft theorem for rapidly rotating vortices. *J. Atmos. Sci.,* **52,** 1829–1833.

——, and R. J. Kallenbach, 1997: A theory for vortex Rossby waves and its application to spiral bands and intensity changes in hurricanes. *Quart. J. Roy. Meteor. Soc.,* **123,** 435–465.

——, V. A. Vladimirov, and P. V. Denissenko, 2002: An experimental study on hurricane mesovortices. *J. Fluid Mech.,* **471,** 1–32.

——, M. M. Bell, S. D. Aberson, and M. L. Black, 2006: Hurricane Isabel (2003): New insights into the physics of intense storms. Part I: Mean vortex structure and maximum intensity estimates. *Bull. Amer. Meteor. Soc.,* **87,** 1335–1347.

Nolan, D. S., and B. F. Farrell, 1999: The intensification of two-dimensional swirling flows by stochastic asymmetric forcing. *J. Atmos. Sci.,* **56,** 3937–3962.

——, and M. T. Montgomery, 2000: The algebraic growth of wavenumber one disturbances in hurricane-like vortices. *J. Atmos. Sci.,* **57,** 3514–3538.

——, and ——, 2002: Nonhydrostatic, three-dimensional perturbations to balanced, hurricane-like vortices. Part I: Linearized formulation, stability, and evolution. *J. Atmos. Sci.,* **59,** 2989–3020.

——, ——, and L. D. Grasso, 2001: The wavenumber-one instability and trochoidal motion of hurricane-like vortices. *J. Atmos. Sci.,* **58,** 3243–3270.

Persing, J., and M. T. Montgomery, 2003: Hurricane superintensity. *J. Atmos. Sci.,* **60,** 2349–2371.

Powell, M. D., and T. A. Reinhold, 2007: Tropical cyclone destructive potential by integrated kinetic energy. *Bull. Amer. Meteor. Soc.,* **88,** 513–526.

Reasor, P. D., M. T. Montgomery, F. D. Marks, and J. F. Gamache, 2000: Low-wavenumber structure and evolution of the hurricane inner core observed by airborne dual-Doppler radar. *Mon. Wea. Rev.,* **128,** 1653–1680.

Reznik, G. M., and W. K. Dewar, 1994: An analytical theory of distributed axisymmetric barotropic vortices on the beta plane. *J. Fluid Mech.,* **269,** 301–321.

Rozoff, C. M., J. P. Kossin, W. H. Schubert, and P. J. Mulero, 2009: Internal control of hurricane intensity: The dual nature of potential vorticity mixing. *J. Atmos. Sci.,* **66,** 133–147.

Schubert, W. H., and B. T. Alworth, 1987: Evolution of potential vorticity in tropical cyclones. *Quart. J. Roy. Meteor. Soc.,* **113,** 147–162.

——, M. T. Montgomery, R. K. Taft, T. A. Guinn, S. R. Fulton, J. P. Kossin, and J. P. Edwards, 1999: Polygonal eyewalls, asymmetric eye contraction, and potential vorticity mixing in hurricanes. *J. Atmos. Sci.,* **56,** 1197–1223.

Smith, R. A., and M. N. Rosenbluth, 1990: Algebraic instability of hollow electron columns and cylindrical vortices. *Phys. Rev. Lett.,* **64,** 649–652.

Terwey, W. D., and M. T. Montgomery, 2002: Wavenumber-2 and wavenumber-*m* vortex Rossby wave instabilities in a generalized three-region model. *J. Atmos. Sci.,* **59,** 2421–2427.

Vladimirov, V. A., and V. F. Tarasov, 1980: Formation of a system of vortex filaments in a rotating liquid. *Izv. Akad. Nauk. SSSR,* **15,** 44–51.

Wang, H., 2002: Rearrangement of annular rings of high vorticity. *Proc. WHOI Summer Program in Geophysical Fluid Dynamics,* Woods Hole, MA, Woods Hole Oceanographic Institution, 215–227.

Yau, M. K., Y. Liu, D.-L. Zhang, and Y. Chen, 2004: A multiscale numerical study of Hurricane Andrew (1992). Part VI: Small-scale inner-core structures and wind streaks. *Mon. Wea. Rev.,* **132,** 1410–1433.